International Journal of Hydrogen Energy 157 (2025) 150321

Contents lists available at ScienceDirect

International Journal of Hydrogen Energy

journal homepage: www.elsevier.com/locate/he

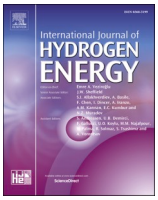

Operando investigation of the two-phase flow behavior of a zero-gap alkaline electrolysis cell using neutron radiography

Stefanie Renz [b,*], Tobias Arlt [c], Nikolay Kardjilov [d], Lukas Helfen [e], Cyrille Couture [e], Alessandro Tengattini [e], Felix Lohmann-Richters [a], Eugen Hoppe [a], Ingo Manke [d], Werner Lehnert [b], Andreas Jupke [f]

[a] Forschungszentrum Jülich GmbH, Institute of Energy and Climate Research, IEK-14: Electrochemical Process Engineering, 52425, Jülich, Germany
[b] RWTH Aachen University, Aachen, Germany
[c] Technische Universität Berlin, Institute of Material Science and Technology, Straße des 17. Juni 135, 10623, Berlin, Germany
[d] Helmholtz-Zentrum Berlin GmbH, Institute of Applied Materials, Hahn-Meitner-Platz 1, 14109, Berlin, Germany
[e] Institut Laue-Langevin (ILL), 71 Avenue des Martyrs, 38000, Grenoble, France
[f] AVT, Fluid Process Engineering, RWTH Aachen, 52074, Aachen, Germany

ARTICLE INFO

Handling Editor: Fanglin F. Chen

ABSTRACT

The two-phase flow behavior inside a zero-gap alkaline electrolysis cell is investigated using operando neutron radiography. The cell was operated with a highly concentrated potassium hydroxide solution. The two-phase flow is evaluated at different electrolyte volume flows, current densities, and temperatures. The amount of gas inside the parallel flow channels is identified and the gas bubble velocity over the channel's length and time is evaluated depending on the different operating conditions. The gas bubble motion requires a high degree of temporal resolution. At the Institut Laue Langevin, a high frame rate of 50 fps was achieved using the NeXT (Neutron and X-Ray Tomograph) neutron imaging instrument, which is fed by the world's most powerful neutron source. This study demonstrates the importance and limitations of high temporal and spatial resolution in neutron radiography for the investigation of two-phase flow in electrochemical flow cells.

1. Introduction

Alkaline water electrolysis (AWE) is a mature technology that is already widely used in industry. Green hydrogen is needed to replace carbon-emitting energy supply via renewable energy sources. For the production of hydrogen, water electrolysis is one of the key technologies and will be needed for large-scale energy storage, transportation, and heat supply in the future. The advantage of alkaline electrolysis over other water electrolysis types is hydrogen production without the need for scarce noble metal catalysts such as iridium or platinum, with the drawback of achieving a lower efficiency compared to, e.g., polymer electrolyte membrane (PEM) electrolysis [1,2].

From a scientific perspective, different strategies are available for enhancing efficiency in AWE, such as increasing the operating temperature [1,3,4] or changing the cell design. The changes in the typical flow cell design aim for better performance due to better strategies for removing gas from the inside of the cell [5]. Gas bubble formation primarily causes two effects within an alkaline electrolysis cell. First, the active surface area of the electrodes is decreased by gas bubbles blocking their active sites. Additionally, gas bubbles decrease the ionic conductivity of the electrolyte, as they form a non-conducting gas void [6].

The development of the zero-gap design was intended to solve these two negative effects by simply leaving no space for the formation of gas bubbles between the diaphragm and electrodes. The gas bubbles were supposed to form on the outer side of the electrodes towards the flow channel, where they could be transported directly out of the cell by the electrolyte solution. It has been known for some time now that the zero-gap design of AWE cells did not entirely fulfill their theoretical purpose of having an ohmic resistance independent of gas bubble formation [7–9]. The ohmic resistance of zero-gap alkaline electrolysis cells is still increasing with increasing current density. Up until today, the effects responsible for the increase in ohmic resistance have been discussed in the literature. Haverkort et al. [8] claim that the front of the electrode, which faces the diaphragm, is not active. They coated it with epoxy and

* Corresponding author.
E-mail addresses: renz.stefanie.sr@gmail.com, stefanie.renz@rwth-aachen.de (S. Renz).

https://doi.org/10.1016/j.ijhydene.2025.150321
Received 29 April 2025; Received in revised form 2 July 2025; Accepted 3 July 2025
Available online 15 July 2025

achieved similar results for electrodes, with and without such a coating. As a possible explanation, they suggested that diaphragm pores might be blocked by gas bubbles, as well as blocked pores in the electrodes due to compression and reduced reactivity caused by local super saturation. Therefore, they suggested a small gap to increase the advection of dissolved gas.

De Groot et al. [7] used simulations to find an explanation for widely varying area resistances mentioned in the literature for the typically used Zirfon diaphragm. Drawing on a simulation they developed, they suggested an uneven current distribution, the blocking of gas bubbles and nano gas bubbles in the diaphragm and electrodes, and possible gaps caused by manufacturing tolerances to be responsible for the losses that occurred.

Hodges et al. [5] developed an alkaline electrolysis cell, which was fed with a KOH solution through the diaphragm, while the gases were released through the electrodes without forming gas bubbles and a two-phase flow of gas and electrolyte solution. This cell exhibited a better performance compared to the conventional flow cell design.

Several strategies exist to mitigate the losses caused by gas bubbles. Few studies have been conducted on decreasing the local surface energy of electrodes by locally coating them with hydrophobic layers of polytetrafluoroethylene (PTFE) in order to lead to a preferred hydrogen gas bubble formation on the hydrophobic surface [10–14]. Liu et al. [15] investigated the gas bubble detachment behavior using a Ni-wire electrode. Especially for the oxygen gas bubbles they found that the gas bubbles might have a tendency to coalescence-induced detachment behavior. They state when detaching coalescence-induced, the gas bubbles introduce disturbance to the concentration boundary layer. Jiang et al. [16] developed an electrode with multichannel pores through laser texturing, that improves the gas transport out of the pores without mitigating the electrolyte transport into the pores.

The development of electrolysis concepts that are gas bubble-free simply avoid gas bubble losses. In the literature, different concepts are available for completely bubble-free electrolysis cells or electrolysis cells with a bubble-free anode. Examples include the use of Gortex-based electrodes [17], conventional gas diffusion layers with pumped electrolyte solutions [18], or capillary-fed electrolysis cells [5] to produce gas directly in gas chambers without forming gas bubbles in the electrolyte solution.

Modifying the surface properties of electrodes can mitigate the influence of gas bubbles on electrolysis performance by adjusting the surface of the electrodes, e.g., to a minimum contact area with the gas bubbles or earlier detachment [19]. The effects of changing the properties of the electrolyte solution by adding surfactants have also been investigated [20]. Gomez et al. [21] summarised that if the electrode surface is hydrophobic, the bubble nucleates to the surrounding of the electrode and the gas bubbles in direct vicinity of the electrode potentially block the ionic pathways which increases the ohmic drop. Whereas, if the electrode properties are hydrophilic the gas bubble will nucleate to the surface of the electrode.

Applying pressure swings [22], magnetic fields [23], centrifugal forces [24], or sound waves [25], as well as an adapted electrolyte volume flow [26], have been tested in the literature in search of effective bubble removal.

All of these reports make clear that gas bubbles have a significant effect on the performance of alkaline electrolysis cells and that huge effort is undertaken to remove them more effectively. However, the two-phase flow behavior inside electrolysis flow cells is not fully understood and most studies do not include a detailed analysis of it. A better understanding of the two-phase flow in electrolysis cells is thus necessary to develop advanced bubble removal concepts.

Therefore, this study investigates the two-phase flow behavior of an alkaline zero-gap electrolysis cell. The focus is on the overall flow behavior of gas bubbles within the entire flow field. The gas layer's thickness was determined and compared to the theoretical gas layer thickness calculated using Faraday's Law. Additionally, the gas bubble velocity was evaluated depending on the point of time during the measurement and location of the gas bubble inside the flow channels. The gas bubble behavior was then interpreted together with the electrochemical results of electrochemical impedance measurements (EIS) and polarization curves.

2. Experimental method

Operando neutron radiography measurements with a zero-gap alkaline electrolysis cell were conducted at the NeXT instrument of the Institut Laue-Langevin (ILL). The neutron source at ILL is the most powerful in the world, which enables a high beam intensity and, consequently, an unprecedented degree of temporal resolution of images. Neutron radiography is a good method for visualizing structures containing light elements like hydrogen and thus water due to the high attenuation, in contrast to most metallic materials, which makes it a good measurement method for the investigation of water electrolysis devices.

2.1. Cell set-up

The investigated cell is an alkaline electrolysis zero-gap cell with an active cell area of 17.64 cm^2 and 14 parallel channels each on the anode and cathode sides (see Fig. 1). The flow channels are placed alternately with channels of the cathode and anode sides, with the channels on one side aligned with the land on the other. The channels of the anode and cathode do not overlap and can both be seen on the resulting images, as shown in Fig. 2. The channel length is 42 mm, with a channel cross-section of 1.5 × 1.5 mm. The used cell consists of two monopolar plates that were mounted onto each other, as shown in Fig. 1. Each of the two monopolar plates was manufactured by milling the parallel flow channels on one side of the plate and onto the back side a pocket was milled in order to improve the neutron transmission. The flow field is equipped with a flow distribution area in a triangular shape so as to distribute the electrolyte solution equally over the parallel flow channels (see Figs. 2 and 10). The electrolyte solution is pumped into the cell by pipes welded to the side of the electrolysis cell. The flow channels are in a vertical orientation and the electrolyte solution flows from the lower cell area to the upper part of the cell. The cell is made from nickel 201. Ni-foam electrodes (*Recemat BV*) were used, with a thickness of 0.3 mm and a specific surface of 5400 m^2/m^3. As the diaphragm, the Zirfon PERL UTP 500 (*Agfa-Gevaert NV*) with a thickness of 500 µm was used. The temperature was controlled by heating rods inserted into the monopolar plates and thermocouples measuring the temperature inside the monopolar plates. Additionally, the electrolyte solution was preheated before entering the cell. The current supply was provided by cable lugs connected to the monopolar plate and the voltage was measured between both monopolar plates. For the power supply, a *Gen20-76* (*TDK*

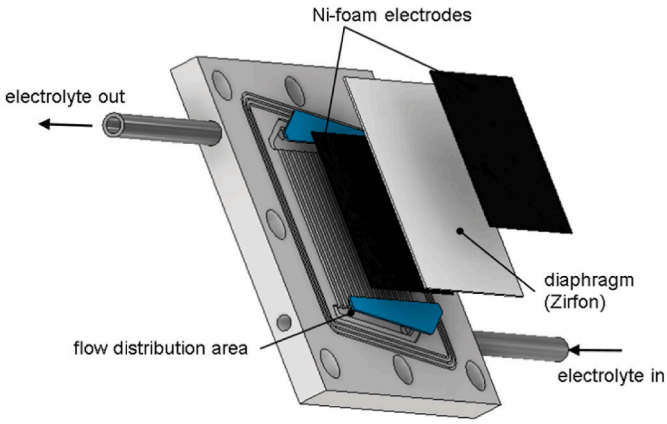

Fig. 1. Flow field plate with electrodes and diaphragm.

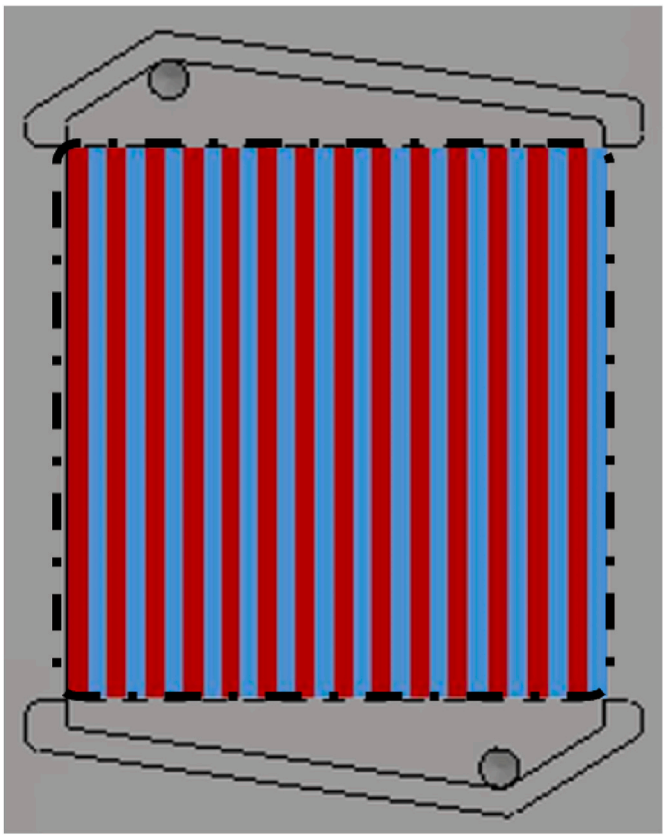

Fig. 2. Flow channels on the cathode (blue) and anode sides (red) with the flow distribution area, point-dashed line is showing the milled pocket on the back. (For interpretation of the references to colour in this figure legend, the reader is referred to the Web version of this article.)

Lambda Germany GmbH) was used and for the EIS measurements, a potentiostat *IM6* (*Zahner Elektrik GmbH & Co. KG*) was used. The electrolyte solution was pumped by membrane pumps of type *Simbdos 10* (*KNF DAC GmbH*).

As the gas formation is the focus of this investigation, the cell was operated in galvanostatic mode (current-driven). The measurements were performed at four different temperatures, namely: 50 °C, 60 °C, 70 °C, and 80 °C, starting from 80 °C and descending. For each of the temperatures, the electrolyte volume flow was set to 100 ml/min, 50 ml/min, 25 ml/min, and 10 ml/min in random order. At every combination of temperature and electrolyte volume flow, a polarization curve was measured starting at 0.01 A/cm^2 and progressing up to 1 A/cm^2 for eight different current densities each. Each time before starting the measurement of the polarization curve, the high frequency resistance (HFR) of the cell was measured at 1 mA/cm^2 and an amplitude of 20 mV (pseudo-galvanostatic mode). In addition, at 80 °C for each used electrolyte volume flow, the HFR was measured at 10 mA/cm^2, 50 mA/cm^2, and 100 mA/cm^2, in order to investigate the influence of gas bubble formation on the ohmic resistance of the cell.

2.2. Neutron radiography measurements

The neutron radiography experiments were performed at the Neutron and X-ray Tomograph (NeXT) instrument at ILL, which is located at a curved neutron guide that transports a high flux (3×10^8 n/cm^{2}s) of cold neutrons (spectrum peak: around 2.8 Å) to the sample position [27]. In order to obtain sufficient beam collimation, a pinhole with a diameter D of 0.03 m was used over a flight path of L = 10 m, defining an L/D ratio of 333. A beam with a squared cross-section of 43 mm was set for the visualization of the alkaline electrolysis cell for through-plane measurements. An indirect detector was used, consisting of a scintillator, mirror, and camera placed in a light-tight box. The scintillator employed was 100 µm-thick ^{6}LiF:ZnS and a sCMOS camera Hamamatsu ORCA-Flash4.0 V2 sCMOS camera, coupled with a 50 mm f./1.2 lens was chosen. The temporal resolution during the measurements was set to 50 fps (exposure time: 20 m s) with a spatial discretization of 91 µm pixel size.

In preparation for the image processing, normalization images were taken. The dark field of the camera sensor was measured by obtaining images without the neutron beam. Reference images with the neutron beam and cell after pumping the electrolyte through the cell before the current was applied (wet images) were then taken. The preparatory images of the cell were used to determine the attenuation coefficient of the liquid using Beer-Lambert's Law.

2.3. Image processing and gas bubble velocity

Image processing was performed using FIJI [28] and distinct plug-ins. Details are given below. The radiographs were normalized with respect to beam intensity fluctuations, beam profile, and other artifacts. Additionally, a slight noise filter (median with a range of 1 pixel in each dimension) was applied. The short range of this filter was selected so as not to suppress small bubbles. As there was still too much noise in the images, threshold-based segmentation was not applicable. We therefore applied the supervised machine learning algorithm WEKA [29] and trained a classifier using typical radiographs of the measurement, whereby the training dataset was less than 1 % of the overall data amount. The obtained classifier was then applied to all hundred thousand radiographs acquired during the measurements. The resulting radiographs now include probabilities for each pixel of belonging to a bubble or not. These results were finally thresholded again to remove all pixels of low probability from an area showing a bubble. The areas of the bubbles are represented by a value of "1" inside the images, whereas no bubble areas are represented by "0." The analysis of bubble motion was undertaken on these images. By multiplying them with the normalized radiographs, the thickness in the beam direction of the bubbles could be quantitatively measured.

2.3.1. Gas bubble velocity

Bubbles could now be easily detected inside the segmented images. To follow the movement of a bubble, the FIJI plug-in TrackMate [30] was fed with own values in terms of estimated bubble sizes, velocity, and direction of movement. Therefore, each radiograph was used, resulting in tracking every 20 m s. TrackMate also measured the coordinates of the barycentric coordinate of each bubble and delivered a trajectory that we then analyzed further.

2.3.2. Gas layer thickness

The gas layer thickness was determined using Beer–Lambert's law. The images resulting from neutron radiography are grayscale. From the gray values of the recorded images by neutron radiography, the gas layer thickness (d_{gas}) could be calculated by means of Equation (1). The preparatory images result in the attenuation coefficient μ and the array of gray values representing the camera noise for each pixel ($T_{dark\ field}$), as well as the array of gray values representing the cell without gas bubbles, filled only with electrolyte solution (T_{wet}). T_{image} is the array of gray values of each pixel of the images recorded during neutron radiography measurements.

$$d_{gas} = -\frac{1}{\mu} \cdot \ln\left(\frac{T_{image} - T_{dark\ field}}{T_{wet} - T_{noise}}\right) \tag{1}$$

3. Results

Polarization curves were recorded at each operation point and EIS measurements were conducted for every temperature – electrolyte

Table 1
Evaluated operation points.

Temperature	Current density	Volume flow
°C	A/cm^2	ml/min
80	0.4	25
80	0.6	25
80	0.4	50
80	0.6	50
50	0.4	25
50	0.6	25
50	0.4	50
50	0.6	50

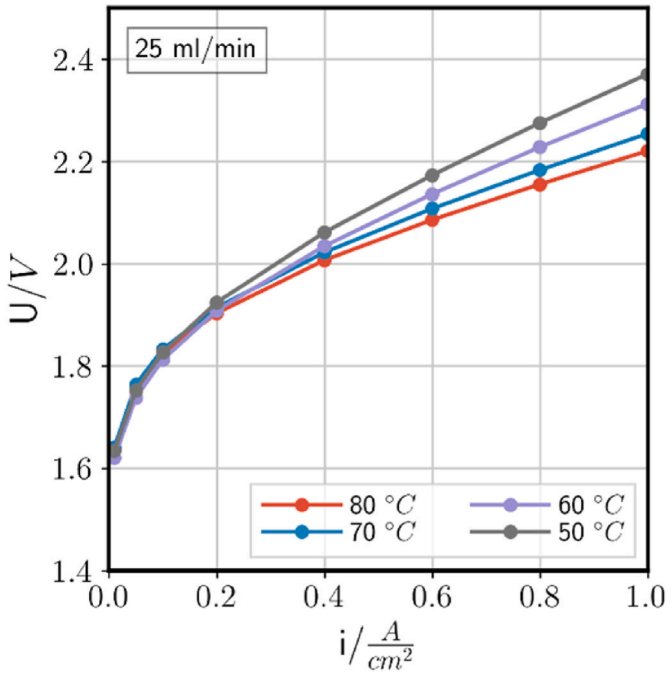

Fig. 3. Polarization curves for temperatures between 50 °C and 80 °C at 25 ml/min electrolyte volume flow.[1].

[1] Polarization curves recorded in Jülich with the exact same measurement set up with a finished break-in process of the cell.

volume flow combination. The electrochemical measurements were performed to characterize the cell and potentially relate the occurring losses to gas bubble behavior inside it.

The pixel size of the recorded images was 91 µm, which means the channel width consists of 16.5 pixels. Gas bubbles smaller than approximately 4 pixels (=0.4 mm) could not be distinguished from pixels showing measurement noise. Unless stated otherwise, the evaluated operation points are the points shown in Table 1. These operation points were chosen from all operation points because of the amount of gas and number of gas bubbles, which were most compatible with the evaluation algorithms used. Operation points at high current densities and high electrolyte flow rates resulted in a churn or annular flow regime in the channels where single gas bubbles could not be identified, whereas operation points at low current and low electrolyte volume flows resulted in too few/small gas bubbles for analysis.

3.1. Electrochemical measurements

The operation points are measured for a duration of 5 min each. For

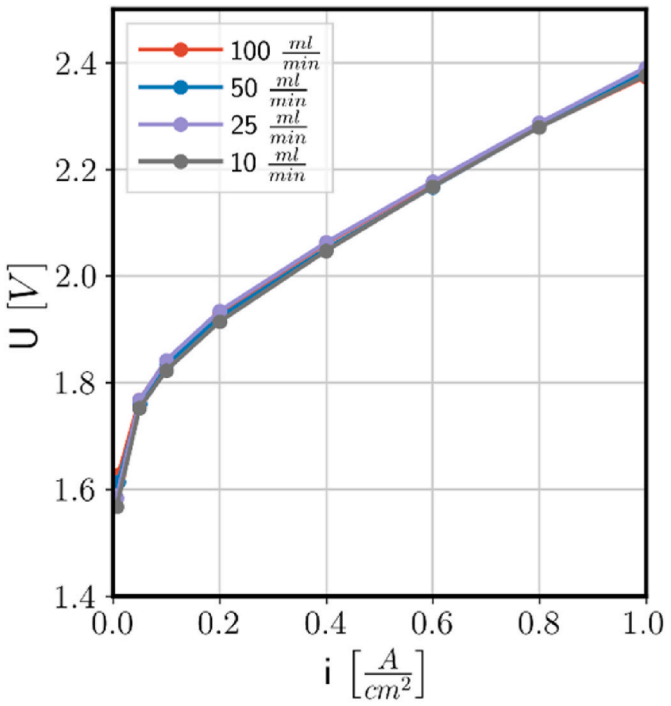

Fig. 4. Polarization curves for 60 °C and flowrates between 10 ml/min and 100 ml/min electrolyte volume flow. [2].

[2] Polarization curves measured at ILL with only a short break-in phase.

the polarization curves, the average of the last minute is taken as steady voltage values. In the literature, it is discussed whether a bubble curtain remains on the electrodes for some time even after switching off the electrolysis operation [31,32]. In this study, all gas bubbles seemed to be transported out of the flow field after turning off the current, which corresponds to the simulation of Rocha et al. [33]. This leads to the assumption that the prior operating conditions are not influencing the latter.

The polarization curves show the typical course of activation losses for small current densities and the linear increase of voltage with increasing current density afterwards representing the total resistance of the cell with its slope (see Fig. 3). No signs of mass transport limitations were observed, which were not expected at a maximum current density of 1 A/cm^2. In Fig. 3, the polarization curves for all temperatures are shown for a 25 ml/min electrolyte volume flow. As expected, the voltage at high current densities decrease with increasing temperature. The electrolyte volume flow seems to have no influence on the polarization curves of the different temperatures, as can be seen in Fig. 4 for different electrolyte flowrates at 60 °C. The findings match with those of Lickert et al. [34], who found the electrolyte volume flow has no influence on the cell performance of a PEM electrolysis cell below 5 A/cm^2. The polarization curves shown in Fig. 3 were not recorded at ILL during the neutron radiography measurements. The granted measurement time was limited and therefore the break-in phase of the electrolysis cell was kept to a minimum, which resulted in higher voltage values for the measurements of 80 °C and 70 °C (the first conducted measurements). As all measurements were conducted in a galvanostatic configuration, however, this had no influence on the gas bubble behavior. Fig. 5 shows that the electrolyte volume flow seems to have no influence on the HFR and, with that, on the ohmic resistance of the cell, shown here for 50 °C as an example. It can also be seen that the electrolyte volume flow does not have an influence on the electrochemical reaction kinetics, because

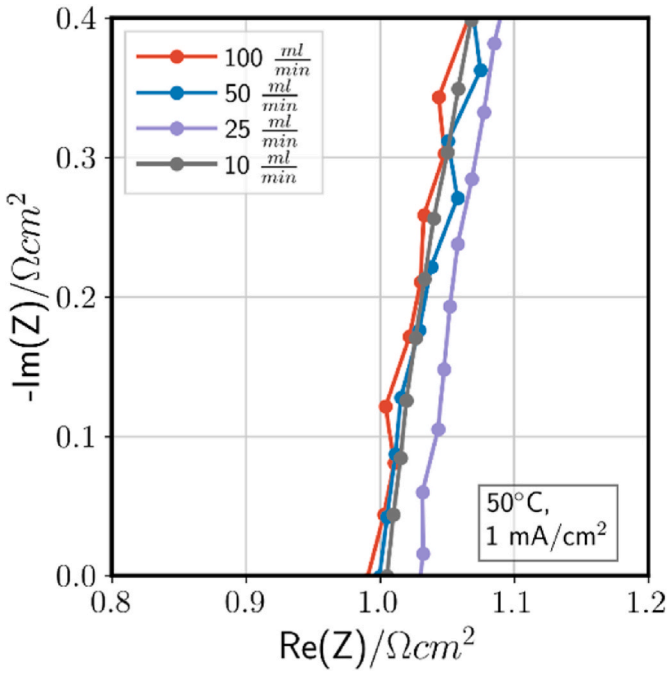

Fig. 5. Electrochemical impedance measurements for a Temperature of 50 °C, measured at 1 mA/cm^2 with an amplitude of 20 mV.

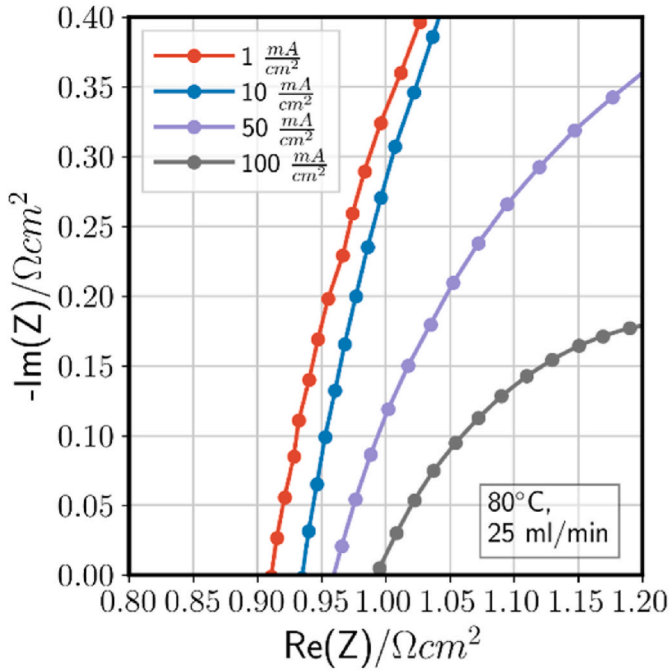

Fig. 7. High frequency resistance of the alkaline electrolysis at 80 °C and 25 ml/min and different current densities.

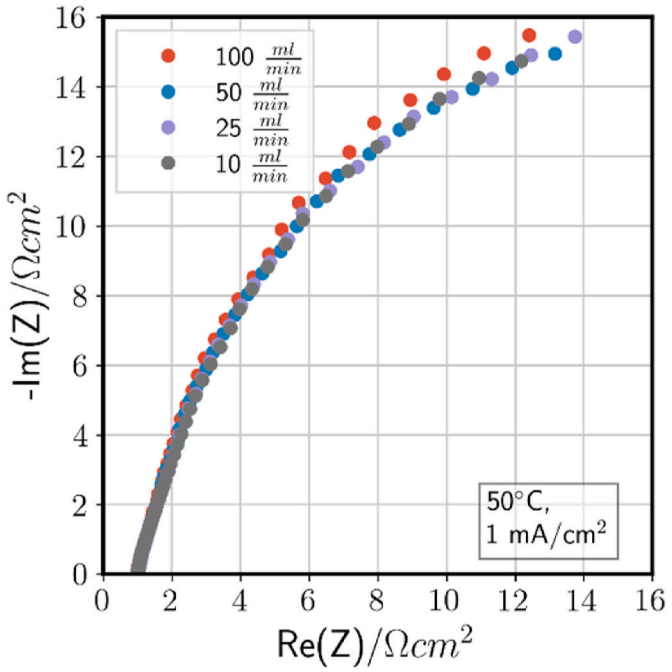

Fig. 6. Electrochemical impedance measurements at electrolyte volume flows at 50 °C and 1 mA/cm^2.

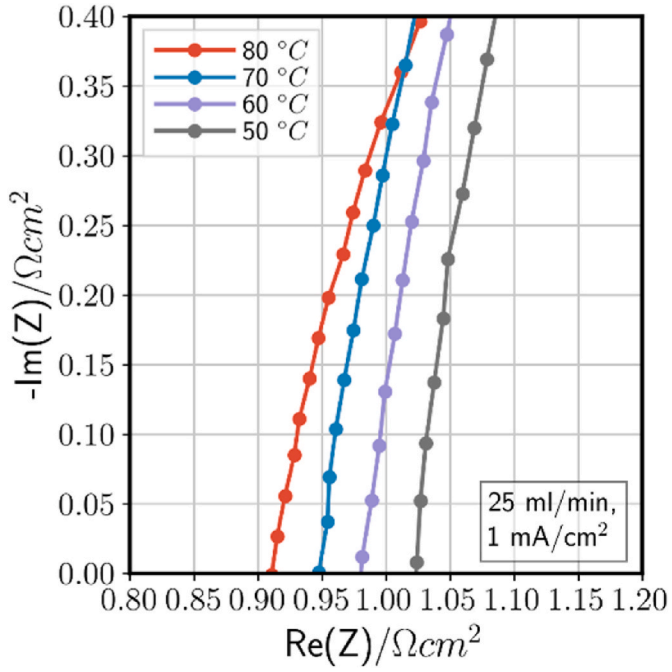

Fig. 8. Electrochemical impedance measurements at different temperatures, 25 ml/min and 1 mA/cm^2.

for all electrolyte volume flow values, the spectra have equal radii of the semicircles (see Fig. 6). The temperature and current density do have an influence on the HFR (see Figs. 7 and 8). The influence of gas bubbles blocking ionic pathways seems to be visible in Fig. 7. The HFR is increasing with increasing current density, which should not be the case if gas bubbles are being removed straight away. The HFR is the ohmic resistance of the cell with the series resistance of the membrane as the biggest contribution. With increasing operating temperatures, the ohmic resistance is decreasing, which is caused by increased ionic conductivity [1,35] (see Fig. 8). The increase in the ohmic resistance with increasing current density is presumably due to the formation of gas bubbles [7–9]. Haverkort et al. [8] investigated the losses of a zero-gap alkaline electrolysis cell using 10 cm^2 of expanded metal electrodes and a Zirfon PERL UTP 500 diaphragm. Their ohmic resistance at 100 mA/cm^2 resulted in 1 Ωcm^2, which is in good accordance with the value obtained here (see Figs. 5–9). In their publication however, the employed electrolyte volume flow was not stated. Efficiency optimised alkaline electrolysis cells with catalyst coated electrodes can reach HFRs of 0.3 Ωcm^2,

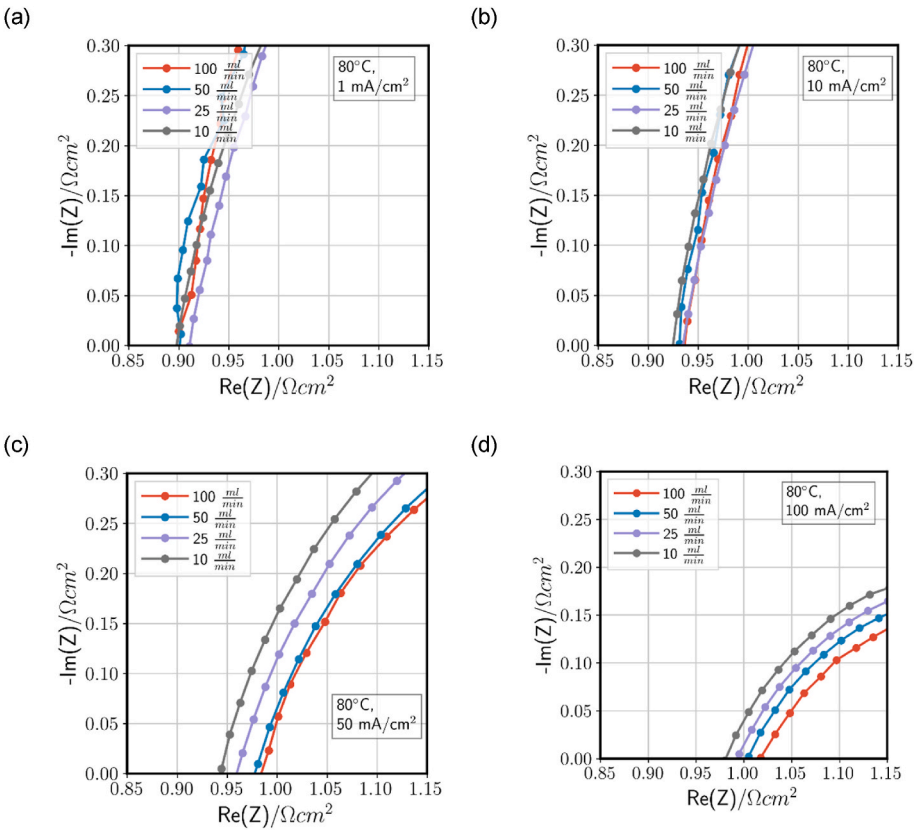

Fig. 9. Influence of the electrolyte volume flow on the high frequency resistance at 80 °C for different current densities.

the main goal in this publication is to investigate the gas bubble behavior.

From Fig. 9, it can be seen that the HFR shows signs of being influenced by the electrolyte volume flow at an increasing current density. At 1 mA/cm^2 and 10 mA/cm^2 (Fig. 9 (a) and (b)), the HFR appears to be the same for all electrolyte volume flows (within measurement fluctuations). For 50 mA/cm^2 and 100 mA/cm^2 (Fig. 9 (c) and (d)), there is a tendency that the ohmic resistance is increasing with increasing electrolyte volume flow. Yuan et al. [36] observed the opposite trend. They claim the reason for an increased ohmic resistance is not the number of gas bubbles or the mass transport overpotential but rather the oversaturation. Their explanation is that if the gas bubble detachment rate is not high enough, the local oversaturation is increasing and therefore the ionic conductivity decreases and the ohmic resistance is increasing. According to Yuan et al. [36], the ohmic resistance should be decreasing with increasing electrolyte volume flow because the gas bubble detachment rate is increasing and therefore the local oversaturation is decreasing. Fig. 9 (c) and (d) show the opposite effect.

The main question regarding the electrolyte volume flow is whether, and if so, how the electrolyte volume flow in the flow channels influences the electrochemical performance in between the electrodes. The difference of the HFR visible from Fig. 9 (c) and (d) would create a voltage difference in between the highest and the lowest electrolyte volume flow of about 5 mV for a 100 mA/cm^2, which would hardly be visible in a polarization curve (Fig. 4) taking measurement noise into account, for 50 mA/cm^2 it would be only 2.5 mV. To investigate the effect further in the following sections we will analyze the gas bubble velocity to compare the electrolyte velocity to the gas bubble velocity to investigate their relationship and to check if the gas bubble velocity seems to be driven by the electrolyte velocity. First however, we will have a look at the gas layer thickness in the flow channels to determine how evenly the gas is distributed throughout the channels to take this factor into account when investigating the electrolyte volume flow, cell temperature and current density and their influence on the cell performance.

3.2. Gas layer thickness

Before starting the evaluation of the images with a constant attenuation coefficient, it was verified that the latter did not change over the 48-h measurement period because of concentration changes within the electrolyte solution. The anolyte and catholyte were not mixed or adjusted during the measurements and therefore the concentration of the potassium hydroxide solution has changed gradually to some extent. The comparison of the attenuation coefficient from the beginning and end of the measurement period, however, did not show any signs of change and therefore is not suspected to have had an influence on the obtained results.

Fig. 10 shows the flow-field orientation of the cell, which matches the orientation on the resulting neutron radiography images. The anode outline is depicted in black and the cathode one in blue. The inlet of the cathode side is located more on the left-hand side and the anode side is mirrored, which leaves the inlet more on the right-hand side in the images.

The resulting distribution of the gas layer thickness is shown for the operation points of 50 °C, 0.4 A/cm^2, 25 ml/min and for 80 °C, 0.6 A/cm^2, 50 ml/min as an example in Figs. 11 and 12. The anode and cathode sides are shown in separate figures to offer a better overview. The results for the gas layer thickness are averaged over 2500 images (=50 s), which are the 50 s of the end phase of the 5-min measurement period of every operation point.

The results of the gas layer thickness distribution over the flow field depends on different operating conditions and are discussed in the following and compared to the literature. Additionally, the elaboration on the influence of the electrolyte volume flow on the gas bubbles inside the flow channels (and therefore the ohmic resistance of the cell), started

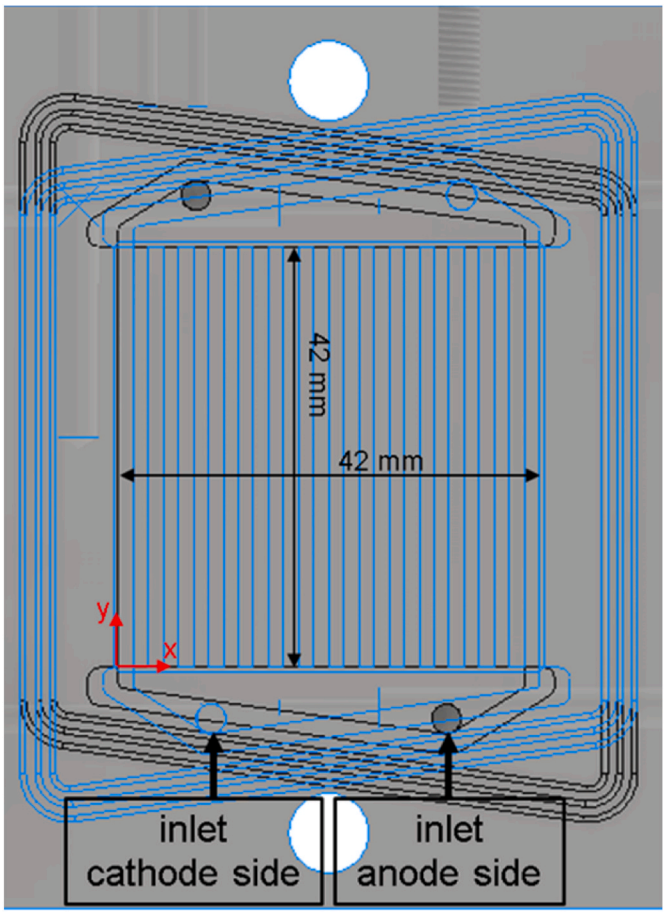

Fig. 10. Cell set-up during neutron radiography measurements with the inlet position of the anode and aathode as shown in the recorded images.

in the subchapter above, will be continued.

From the images in Figs. 11 and 12, it can be observed that the average gas layer thickness is greatest in the upper corners opposite the respective outlet. Buoyancy and coalescence of forming gas bubbles leads to more gas in the upper part of the flow-field. At higher current densities, the overall gas layer is thicker because more gas is being produced. Moreover, the overall gas layer of the cathode flow channels is thicker because twice as much gas is being produced compared to the anode side. For the same current density, the overall gas layer thickness seems to be increasing with increasing temperature, supposedly because the gas solubility is decreasing with temperature [37].

To understand the gas layer thickness or gas distribution in relation to electrolyte volume flow, current density and temperature, it is important to take the effects inside the cell into account. As the literature investigating the two-phase flow of alkaline electrolysis cells is scarce, the flow effects are compared to flow investigations conducted for PEM electrolysis. The difference between the two electrolysis types is that PEM is using pure water instead of potassium hydroxide as the electrolyte solution, which results in a difference of surface tension and contact angle at the three-phase boundary of the channel material, liquid electrolyte, and gas bubble, respectively. The porous transport layer (PTL) in alkaline electrolysis cells is usually nickel-based, whereas the PTL material in PEM cells is typically titanium-based. The second relevant difference is the necessity of a functioning hydroxide ion transportation capacity through the electrolyte solution for alkaline electrolysis cells, which can be mitigated by gas bubbles. A PEM electrolysis cell is using a proton conducting membrane. Nonetheless, the flow effects occurring in the flow field of an alkaline electrolysis cell are comparable to those occurring in the flow field of a PEM cell (the flow

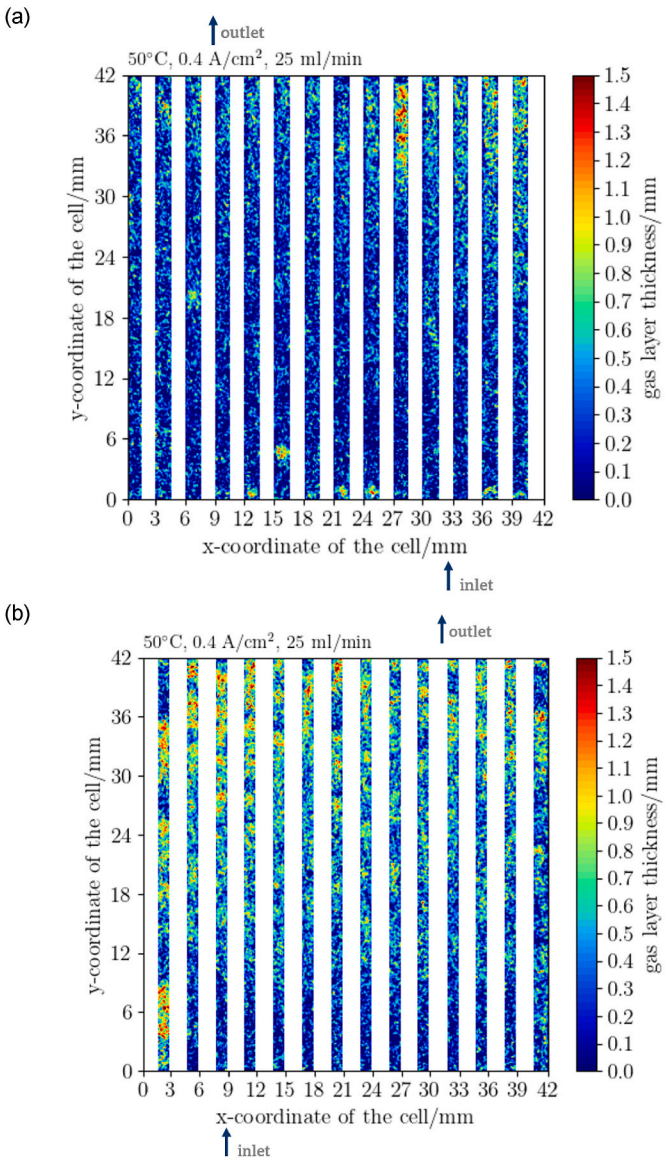

Fig. 11. Gas layer thickness at the operating point of 50 °C, 0.4 A/cm^2, and 25 ml/min in the anode flow channels (a) and cathode flow channels (b).

effects are compared to the anode side of PEM electrolysis cells, given that mostly no electrolyte is supplied to the cathode side) [36].

In the following the gas layer thickness and published literature is used to imply how evenly the electrolyte volume flow is distributed throughout the flow field without actually being able to measure it to get a better understanding how the electrolyte flow in the flow field affects the electrochemical performance of the cell.

According to Leonard et al. [38], the electrolyte volume flow has little or no influence on the gas bubble diameter but on the gas bubble's detachment rate. This potentially leads to a shift in transitioning from one flow regime to the other. A higher electrolyte volume flow can therefore decrease the ohmic resistance according to Yuan et al. [36], because the local oversaturation is decreasing due to more gas bubbles detaching earlier and being transported out of the flow field. The investigation of Majasan et al. [39] shows that flow channels with a higher electrolyte flow rate have the tendency to contain smaller gas bubbles, whereas the flow channels with a lower electrolyte flow rate tend to contain gas bubbles with a bigger diameter or gas slugs. The flow field geometry utilized by Majasan et al. [39] is similar to the flow field geometry employed in this investigation. Their flow field used parallel

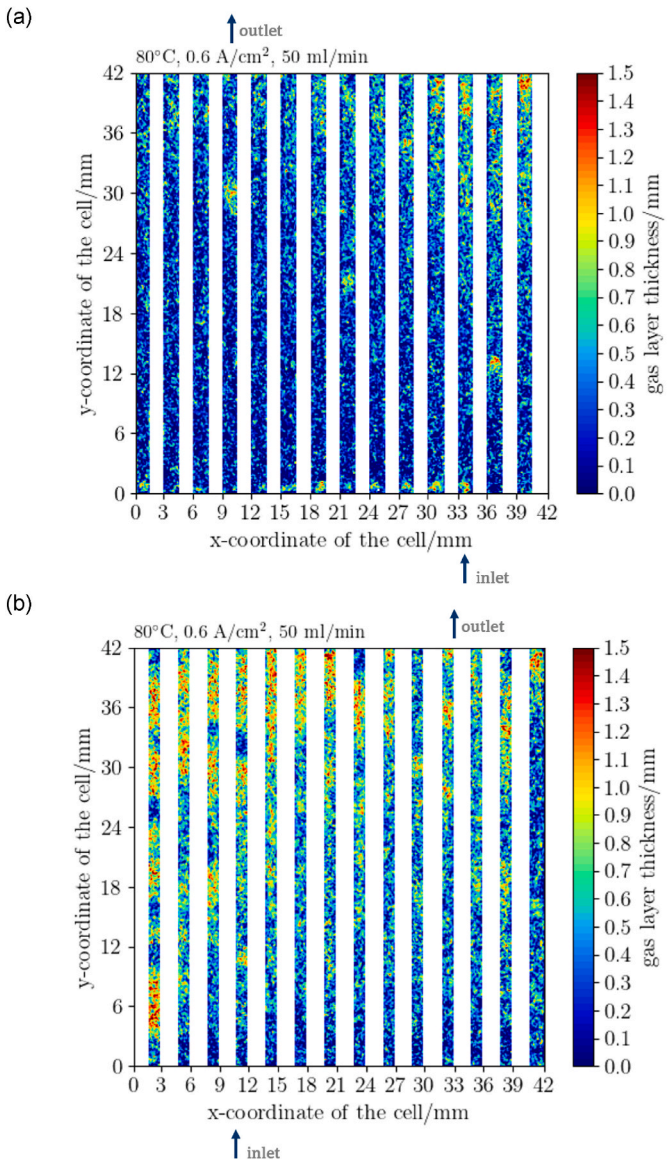

Fig. 12. Gas layer thickness at the operating point of 80 °C, 0.6 A/cm^2, and 50 ml/min in the anode flow channels (a) and the cathode flow channels (b).

flow channels and the electrolyte was distributed in a similar way. Due to the flow field design using parallel flow channels, the electrolyte flow rate was not equally distributed inside the flow channels. Wang [40] describes the behavior of the electrolyte flow at a T-junction. At low Reynolds numbers (low flow velocities), the flow is equally divided into two separate streams. At increasing Reynolds numbers (increasing flow velocities), the arm without change (in our case less change) in directions is supplied with a higher volume flow because of inertia. For the flow field geometry used here, this means that by increasing the electrolyte volume flow, more of the electrolyte solution is transported along the arms of the flow distribution triangle because of inertia, creating a higher electrolyte supply to the flow channels close to the inlet, respectively, right at the end of the longer arm opposite the side of the electrolyte inlet, with less distributed to the other flow channels. Majasan et al. [39] observed that with increasing current density, a more unique electrolyte velocity over the flow channels became apparent, which they explain with a decreasing pressure loss with increasing gas content of the two-phase flow. Their observation leads to an almost equally distributed electrolyte flow within the flow channel for current densities greater than 1 A/cm^2; for lower current densities, the non-uniform electrolyte flow distribution persists. The gas layer thickness in the flow field used here is thickest for the upper corner located on the side where the flow inlet is located. Maier et al. [41] used the same PEM cell as Majasan et al. [39] and investigated the water thickness of the GDL on the anode side for different GDL materials. In their investigation, the GDL had the thinnest water layer (thickest gas layer) in the upper right-hand corner, which Majasan et al. [39] identified as the channel with the highest flow velocity. According to Wang [40], for the geometry of the inlet area used here, the electrolyte volume flow should result in a higher volume flow in the outer flow channels, which then, according to Majasan et al. [39], should result in a lower gas layer thickness in these channels. As this does not apply to the observations in Figs. 11 and 12 a closer examination was made of the similarities and differences of the cell used by Majasan et al. [39] and Maier et al. [41] and the cell used here. As the gas layer thickness was mainly in one corner of the cell, which is opposite the two-phase flow outlet of the flow field, it seems obvious that the gas distribution is not only dependent on the geometrical factors of the inlet and the channel's geometry but also on the outlet. In this cell, the longer arm of the outlet area appeared to create a bottleneck for the gas bubbles to leave the flow outlet area. The water layer investigations of Maier et al. [41] seem to show the same effect for their channel closest to the outlet. In their findings, the outlet channel into which all flow field channel drained their gas–electrolyte mixture was supposedly filled up with gas from left to right, which made it harder for the last channels to push the gas out.

A higher electrolyte volume flow inside the channels decreases the local oversaturation and therefore increases the ionic conductivity, such that the local gas amount produced is increasing and the gas layer is getting thicker. With a thicker gas layer, the conductivity is decreased. The steady state condition of these two contradicting effects seems to shift with higher flowrate towards a lower gas layer thickness (see Figs. 15–18). The buoyancy and coalescence of forming gas bubbles leads to more gas in the upper part of the flow field. At higher current densities, the gas layer is thicker because more gas is being produced. The gas layer of the cathode flow channels is also thicker because twice as much gas is produced compared to the anode side. For the same current density, the gas layer thickness is increasing with temperature, because the gas solubility is decreasing with it [37]. Comparing the same operation point with different electrolyte volume flows (see Figs. 15–18), there are contradictory tendencies with respect to the influence on gas layer thickness. The potential reason for this is that at higher electrolyte volume flows, the gas bubbles detach at a smaller gas bubble size. As small gas bubbles could not be identified in the neutron radiography images because they could not be distinguished from measurement noise, the gas layer might appear to have been thinner. However, even if that was the case, from the impedance it can be seen that the ohmic resistance was slightly increasing with increasing electrolyte volume flow. The visual results and impedance measurements seem to show both an opposite effect to what is described by Yuan et al. [36]. If the rate of gas transported out of the flow field and forming gas is changed to more gas being present in the flow channels, it would result in a higher ohmic resistance, which is supported by gas being present at lower positions in the flow channels (see Figs. 11 and 12). The polarization curves in Fig. 4 show that the performance does not seem to be effected by more or less gas being present in the flow channels with different electrolyte volume flowrates and the EIS spectra for current densities equal or higher 50 mA/cm^2 show only a low dependency of 5 mV difference between 10 ml/min for 80 °C and 100 mA/cm^2 and only 2.5 mV difference at 50 mA/cm^2 (see Fig. 9 (c) and (d)). A possible reason to why a higher electrolyte volume flow is increasing a slight decrease in temperature.

The averaged gas distribution in the flow channels shows that the gas distribution in the flow channels is dependent on the electrolyte volume flow (see Figs. 11 and 12). This implies that the electrolyte volume flow is not equally distributed in the flow channels. Supposedly, the areas with a larger gas content have a lower electrolyte volume flow compared

to the areas with a lower gas content, which shows that using neutron radiography with the used temporal resolution is giving an idea about the distribution of both phases of the two-phase flow (assuming the gas production is distributed equally over the flow field). The electrolyte volume flow distribution will be further discussed in the next subsection using the results from the gas bubble velocity distribution in the flow field.

An existing gap between the theoretical gas layer thickness and the measured one can also be seen in Fig. 13. Fig. 13 (a) shows the measured gas layer thickness dependent on the current density, which can be compared to the theoretical, calculated gas layer thickness shown in Fig. 13 (b). The gas layer thickness dependent on the position (y) in the channel can be calculated with Equation (2), which uses the ratio of the gas volume inside the cell (V_{gas}) divided by the active channel area (A), which is equivalent to the active cell area. The gas volume (V_{gas}) is exchanged for the total volume of the flow channels (V_{tot}) multiplied by the ratio of gas volume flow ($\dot{V}_{gas}$) and total volume flow consisting of the gas volume flow ($\dot{V}_{gas}$) and electrolyte volume flow ($\dot{V}_{KOH}$). The gas volume flow is multiplied by the Faraday efficiency (η_F), which is assumed to be 100 % in an electrolysis cell.

$$d_{gas,theo.}(y) = \frac{V_{gas}(y)\cdot\eta_F}{A(y)} = \frac{\dot{V}_{gas}(y)\cdot\eta_F}{\dot{V}_{gas}(y)\cdot\eta_F + \dot{V}_{KOH}} \cdot \frac{V_{tot}(y)}{A(y)} \tag{2}$$

The values shown in Fig. 13 (b) are the mean gas layer thickness values ($\overline{d_{gas}}$) and are calculated by Equation (3) using the fraction of the mean gas volume flow ($\overline{\dot{V}_{gas}}$) divided by the mean total flow of gas and electrolyte ($\overline{\dot{V}_{gas}}\cdot\eta_F + \dot{V}_{KOH}$) multiplied by the total volume (V_{tot}) to obtain the mean gas volume ($\overline{V_{gas}}$). The mean gas volume ($\overline{V_{gas}}$) divided by the active cell area (A) yields the mean gas layer thickness ($\overline{d_{gas}}$). The mean gas volume flow ($\overline{\dot{V}_{gas}}$), calculated by Equation (4), is determined using Faraday's law (z_{H_2/O_2}: transferred electrons, j: current density, F: Faraday constant, b: width of the flow field, V_m: molar volume) integrated over the channel length (L). Figs. 11 and 12 show that the gas layer thickness is not equal throughout the channel and does not behave in the same manner from one channel to another. The reason for this is that the transient conditions of gas forming and accumulating along the channel length leads to different residence times of the gas and different degrees of coalescence. Equations (3) and (4) average the effect of forming gas over the channel length by using the mean gas volume. All other described influence factors (coalescence, buoyancy, etc.) mentioned previously are neglected here.

$$\overline{d_{gas}} = \frac{\overline{\dot{V}_{gas}}\cdot\eta_F}{\overline{\dot{V}_{gas}}\cdot\eta_F + \dot{V}_{KOH}} \cdot \frac{V_{tot}}{A} \tag{3}$$

$$\overline{\dot{V}_{gas}} = \frac{1}{L}\int_0^{y=L}\left[\left(\frac{1}{z_{H_2}} + \frac{1}{z_{O_2}}\right)\cdot\frac{jb}{F}\cdot V_m\right]dy \tag{4}$$

Especially for low current densities, the deviation between the calculated and measured gas layer thickness is high and is decreasing for increasing current density. At higher current densities, the gas layer thickness appears to become linear but a deviation between the calculated and measured gas layer thickness remains.

There are several possible reasons for the deviation, which are discussed in the following in detail. The conducted measurements were performed in a current-driven manner, which means that effects on the cell efficiency like changing ionic conductivity or electrode overpotentials can be ruled out as possible causes. For each applied current density, the same amount of gas and therefore the same averaged gas layer thickness should be produced by the cell. However, the calculation is assuming 100 % Faraday efficiency. If this assumption is not accurate this could, at least partially, be responsible for the deviation. Another possible cause of the deviation is the assumption made in the theoretical calculation of the gas layer thickness, that at each location within the flow channel the same amount of gas is produced over time. Local or temporal deviations of the gas production are not accounted for. The measurement method might also be a possible cause of the deviation shown. As already noted, small single gas bubbles are not possible to distinguish from measurement noise, which could result in a lower gas layer thickness. Deviations could be a result of the measurement method itself and the way in which the images are created during neutron radiography measurements and the accuracy of the baseline images, as well as filter, subsequent image processing influences, and the image blurring due to finite spatial resolution.

For smaller current densities, it is likely that the cause of the deviation in Fig. 13 (a) and (b) is small gas bubbles being mistaken for measurement noise. A main component of the deviation, however, is suspected to be caused by the neglected influence of gas solubility, buoyancy, and coalescence, which prompts the gas layer thickness to be thinner than calculated by Equation (3).

3.3. Gas bubble velocity and number

The gas bubble velocity and formed number of gas bubbles is primarily a function of the influencing factors of current density, electrolyte volume flow, temperature, geometry, and the material (dimensions

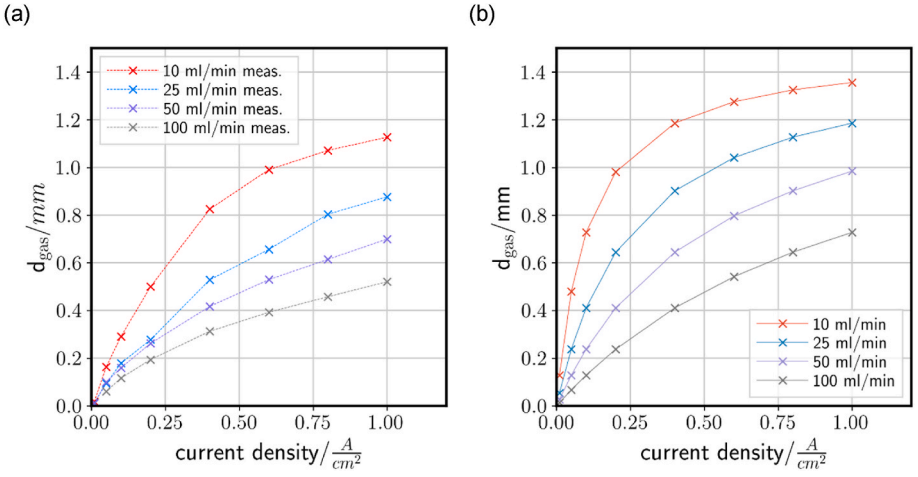

Fig. 13. Measured gas layer thickness (a) compared to the calculated gas layer thickness by Equation (2); (b) for a temperature of 80 °C and different electrolyte volume flows.

and friction) of the flow field. Below, the observations regarding the gas bubble velocity and the number, dependent on these influencing factors, is described, explained, and compared to the findings of other published investigations as well as the electrochemical results shown in section 3.1.

A typical gas bubble velocity is shown in Fig. 14 (a) for 50 °C, 0.4 A/cm^2, 25 ml/min, and Fig. 14 (b) 80 °C, 0.6 A/cm^2, 50 ml/min. The anode and cathode flow channels are shown in one figure, but were evaluated separately. The anode flow channels have a dark gray background, whereas the cathode flow channels have a white one (see Fig. 14). Each flow channel is divided into segments of 2 mm in length. In each of these segments the bubble velocity is averaged over all the bubbles tracked in the segment within the analyzed duration of 5 min (=15,000 images). The number of points indicates the number of bubbles tracked in each segment. The velocity is tracked for every second flow channel for the anode and cathode in order to prevent the algorithm within TrackMate from detecting moving objects crossing channel borders and falsifying the result. The comparison of the velocity distribution over the flow channels of the flow field, with the set of the other remaining channels leading to a similar velocity distribution, which is why the analysis was performed with every second channel of the flow field. The resulting mean gas bubble velocities are in the range of 0 mm/s and 50 mm/s for electrolyte volume flows of 25 ml/min and 50 ml/min. Gas bubbles are depicted in light gray if the mean velocity results in a negative value. This primarily occurred at the end or beginning of the flow channels if gas bubbles were stuck for a moment and oscillated with the oscillation

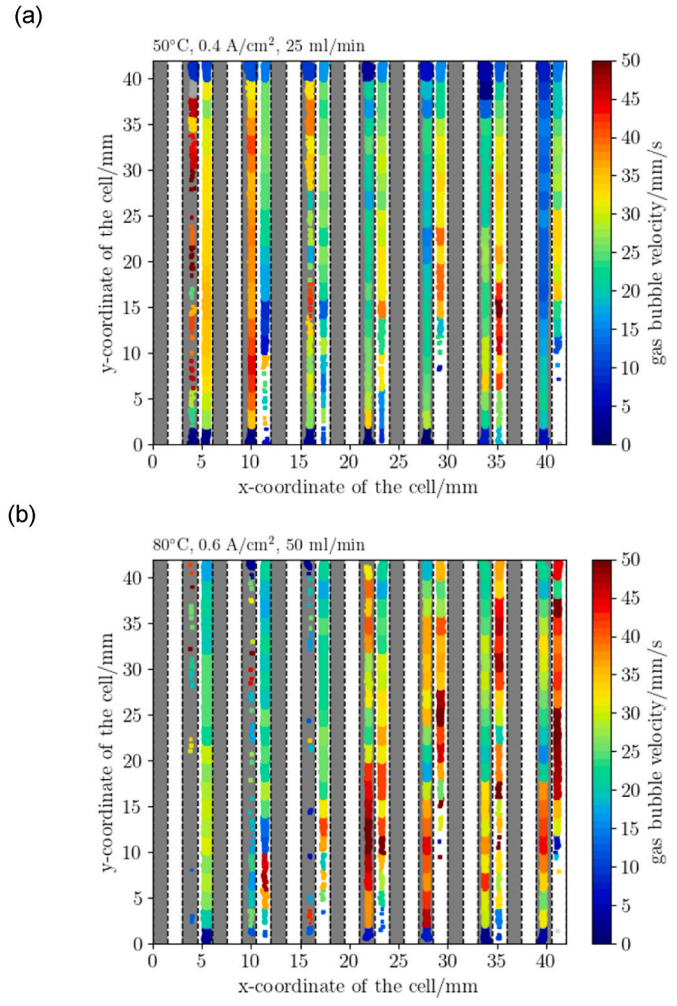

Fig. 14. Gas bubble velocity for every second flow channel for 50 °C, 0.4 A/cm^2, 25 ml/min (a) and 80 °C, 0.6 A/cm^2, 50 ml/min (b).

of the electrolyte membrane pump. The TrackMate algorithm mistakenly identified these gas bubbles as different ones with movement in a negative y-direction.

The gas bubble velocity and number are both described together. In Fig. 14, the number of points does not describe the total number of gas bubbles, as gas bubbles moving through several segments, are shown as several points. Therefore, the total number of different gas bubbles detected can be seen in Table 2 for each operating point, together with an averaged velocity determined for the cathode and anode sides separately.

Comparing the differences in gas bubble velocities caused by different current densities for different operating points, it appears that the detected gas bubbles at higher current densities start slower at a low y-coordinate. The slower gas bubble velocity might be caused by the greater gas amount produced at higher current densities. The greater gas amount is likely to cause more coalescence already at low y-coordinate of the flow channels. To some extent, the transportation of gas out of the flow channels might even experience some resistance due to the two phase flow from all channels need to go through one outlet, which might be the reason why the velocity drops before the flow exits the channel. With higher current density, more gas bubbles are detected at a low y-coordinate in the flow channels. In the neutron radiography images, gas bubbles must attain a certain size to be distinguished from measurement noise, and therefore more gas bubbles can be detected at higher current densities. The gas bubbles are already bigger at low y-coordinates at higher current densities. Other than that, the current density does not appear to have a significant influence on the gas bubble velocity or the mean gas bubble velocity on the anode and cathode sides. In contrast to the observation made here, Majasan et al. [39] observed a linear increase in the gas bubble velocity at a current density range comparable to the range of this evaluation. They explained the increasing gas bubble velocity with increasing current density by a lower pressure drop on the basis of increasing amounts of gas in the electrolyte solution.

Different electrolyte volume flows led to a completely different two-phase flow distribution within the flow field. Operating points at different current densities but the same temperature and same electrolyte volume flow appear similar when it comes to the gas bubble velocity distribution and gas bubble number over the flow field. The electrolyte volume flow directly influences the gas bubble velocity, with a slower electrolyte volume flow resulting in a slower drag on the gas bubbles affected by it. From Fig. 14, it can be seen that the gas bubbles are first detected at a greater y-coordinates at a higher electrolyte flow rate compared to the lower flow rates. The electrolyte volume is linked to the detachment diameter of the gas bubbles. The higher the electrolyte volume flow, the earlier the gas bubbles are detached. At a small gas bubble diameter, they cannot be detected in the neutron radiography images and have less wall friction because of their size. A smaller gas bubble size might explain why gas bubbles start to be detected at higher y-coordinates in the channels compared to lower electrolyte volume flows. Majasan et al. [39] observed a better performance at higher electrolyte volume flows, which they assumed to be because of better reactant availability, better heat supply, and a shorter slug length. This effect was not observed in our investigation, whereas Majasan et al. [39] only saw this effect for higher current densities than the ones used here. Assuming an equally distributed electrolyte volume flow through the flow channel without gas production would result in a flow velocity of 24.12 mm/s for 25 ml/min and 48.18 mm/s for 50 ml/min. Considering that the electrolyte is not equally distributed and that the flow channel volume also contains gas, the electrolyte flow velocity should at least in some flow channels be a lot faster than the here calculated value. The resulting gas bubble velocities seem to be to an extend slower than the electrolyte flow. The gas bubble velocity profile being slower at low y-coordinates, accelerated towards the middle of the channel and then decelerated again towards the end, also seems to be an indicator that the gas bubble velocity in the flow channels is not directly linked to the electrolyte volume flow.

Table 2
Mean velocity and number of detected gas bubbles, as evaluated by TrackMate.

			Anode		Cathode	
Temperature	Volume Flow	Current Density	Mean Velocity	Number of detected Gas Bubbles	Mean Velocity	Number of detected Gas Bubbles
°C	ml/min	A/cm^2	mm/s	–	mm/s	–
80	50	0.4	26.14	1527	26.37	18,513
80	50	0.6	24.05	4309	23.49	32,081
80	25	0.4	10.32	13,972	18.5	39,983
80	25	0.6	10.91	7543	11.56	19,599
50	50	0.4	12.02	3281	21.48	57,626
50	50	0.6	12.08	2271	22.21	42,272
50	25	0.4	11.12	7232	24.96	31,429
50	25	0.6	14.21	14,129	23.69	42,112

The temperature has an influence on the gas bubble velocity distribution over the flow field as well. The gas bubble velocity distribution changes for each operating point with a change in temperature. At 80 °C the gas bubble are starting at a lower y-coordinate compared to 50 °C. This phenomenon was mentioned previously as an observation caused by the current density. The behavior of the gas bubble velocity inside the flow channels caused by the temperature does not seem intuitive. However, with increasing temperature, the gas solubility decreases, which means that less gas is dissolved in the electrolyte solution and more gas is present in the gas phase. Additionally, the density of both gases is decreasing with increasing temperature, but so is the density of the electrolyte solution, which leads to a decreased buoyancy at an increasing temperature. To fully understand the effect of the temperature on the gas bubble velocity, further measurements will be necessary.

The geometry of the flow field and especially the flow distribution area and electrolyte inlet position has an influence on the gas bubble velocity and the gas bubble behavior in general. On the opposite side of the electrolyte inlet, fewer gas bubbles were identified and the first detection of gas bubbles mostly starts at higher y-coordinates of the flow channels. The gas bubble velocity distribution in all flow channels shows that the velocity fluctuates across the flow channel. By looking at every single channel, the gas bubble velocity is low at low y-coordinates and increases with phases of decreasing velocity. From a certain height of the flow channels, the flow velocity decreases again with phases of increasing gas bubble velocity. The y-coordinate from where the velocity of the gas bubbles increases again also seems to be dependent on the location of the flow outlet. The y-coordinate where the slowing down of the gas bubbles start seems to be greater for flow channels located closer to the flow outlet. The velocity variation along the channels might also be related to the pump and variation of the bubble–wall interaction. In the literature, the oscillation of most electrolyte pumps and its effect on two-phase flow behavior is rarely discussed. However, as the bubble velocities are analyzed from images averaged over 5 min, it appears unlikely that the oscillation stems from the frequency of the membrane pump, which is in the range of a second. A more likely explanation is that gas bubbles are accelerated by the electrolyte volume flow and buoyancy and decelerated once they coalesce with other gas bubbles due to wall interaction and a supposedly slower discharge of larger gas bubbles. Gas bubbles that form at lower y-coordinates in the channels reach higher velocities throughout. The reason for this is that they are smaller and therefore have less wall friction. Additionally, there is less gas lower in the flow channels and therefore coalescence is less frequent.

From the number of detected gas bubbles, it can be seen that a lot fewer gas bubbles are detected on the anode side compared to the cathode one. For 25 ml/min, the difference is 2.5–4 times less. The difference is even greater between both sides at a higher volume flow, at 50 ml/min (between 7 and 19 times lower). The lower number of detected gas bubbles, especially at higher electrolyte volume flows, can be explained with an earlier detachment at higher electrolyte volume flows. To some extent, the difference might also be caused by the limitation of being able to identify small gas bubbles in the neutron radiography images.

The gas bubble velocity shows a dependency on the electrolyte volume flow. Even though the gas bubbles are not being dragged along with the approximate same velocity than the electrolyte flow, especially with the gas bubble velocity being accelerated throughout the first half of the flow channels and decelerated during the upper half. But the average gas bubble velocity appears to be higher with a higher electrolyte volume flow. However, the electrochemical performance seems not to be influenced by the electrolyte volume flow, which might suggest that the electrolyte volume flow in the flow field has little to no influence on the electrochemical performance in between the electrodes for a volume flow in between 10 ml/min and 100 ml/min (see Fig. 4). Although the EIS measurements show a slight increase in series resistance with increasing electrolyte volume flow, with a minor effect on voltage (for 50 mA/cm^2 and 100 mA/cm^2, see Fig. 9 (c) and (d)).

4. Summary and conclusions

New generation neutron radiography and tomography fed by powerful neutron sources make it possible to investigate devices like electrolysis cells with a high degree of temporal and spatial resolution. In this study, a temporal resolution of 0.02 s was reached with a spatial resolution of 0.4–0.6 mm. Such measurement methods are ideal to shed light on what two-phase flow effects are taking place inside the cell and therefore help to increase the efficiency of electrolysis cells. Using two-dimensional radiography images, it is possible to identify the gas layer thickness and draw conclusions regarding the amount of gas within cells with the advantage of obtaining a higher temporal resolution compared to tomographic measurements. The drawback compared to tomographic images is that it is not possible to identify the layer in the beam direction, where the gas bubbles are, nor to distinguish how much gas is in the foam electrodes, diaphragm, and flow channels. Moreover, there is a tradeoff between tomographic investigation of a cell with detailed information on the gas bubble location and temporal information captured by radiography imaging.

This investigation proves the feasibility of investigating electrolysis cells with the temporal resolution needed to resolve the two-phase flow in a sufficient manner and guides the way towards solving many unanswered questions regarding flow phenomena inside electrolysis cells. Utilizing the obtained images, the gas layer thickness was determined at different operating conditions. The following conclusions can be drawn:

- The gas layer thickness increases with increasing temperature, which is most likely related to gas solubility.
- The gas layer thickness increases with increasing current density because more gas is produced, which influences the series resistance to increase with increasing current density, likely due to a blockage of ionic pathways due to gas bubbles.
- The influence of the electrolyte volume flow on the gas layer thickness shows contradictory tendencies. The electrochemical

measurements however show a slight influence on the series resistance, the series resistance is increasing with increasing electrolyte volume flow.

Additionally, the gas bubble velocity and gas bubble distribution within the flow channels were determined and the following results were obtained:

- The electrolyte inlet and outlet design and location substantially influence the two-phase flow within the flow channels.
- The temperature and electrolyte volume flow have a substantial influence on the gas bubble velocity and gas bubble distribution.
- The current density does not seem to have an influence on the gas bubble velocity other than gas bubbles being jammed at the outlet and therefore slowed down.
- The gas bubble velocity does not appear to be constant or linear, but fluctuates spatially.

This investigation shows where gas bubbles are formed in the flow field, how many are being formed and how fast they are being transported out of the cell. However, from the gas bubble behavior in the flow field the gas bubble resistance influencing the cell performance could not be seen. Neutron radiography with a temporal resolution up to 0.02 s can be a powerful tool to investigate the gas evolution at the electrodes and how it is being transported through the gas diffusion layer into the flow field. This investigation is the first step of a better understanding of the gas formation and transport out of the cell.

CRediT authorship contribution statement

Stefanie Renz: Writing – original draft, Visualization, Software, Methodology, Investigation, Formal analysis, Data curation, Conceptualization. **Tobias Arlt:** Writing – review & editing, Writing – original draft, Visualization, Software, Data curation. **Nikolay Kardjilov:** Writing – review & editing, Writing – original draft, Visualization, Software, Data curation. **Lukas Helfen:** Writing – review & editing, Data curation. **Cyrille Couture:** Data curation. **Alessandro Tengattini:** Writing – review & editing, Data curation, Conceptualization. **Felix Lohmann-Richters:** Writing – review & editing, Conceptualization. **Eugen Hoppe:** Writing – review & editing, Data curation. **Ingo Manke:** Writing – review & editing, Conceptualization. **Werner Lehnert:** Writing – review & editing, Resources, Conceptualization. **Andreas Jupke:** Writing – review & editing.

Declaration of competing interest

The authors declare that they have no known competing financial interests or personal relationships that could have appeared to influence the work reported in this paper.

5 Acknowledgements

The authors would like to thank Walter Zwaygardt (Forschungszentrum Jülich) and Edward Rauls for their support in conducting the neutron radiography measurements and their help with the preparation. Furthermore, we are grateful to Birgit Schumacher, Bernd Pelzer, Andreas Maintz, and Thomas Pütz (Forschungszentrum Jülich) for their help during the preparatory phase and the fruitful discussions that ensured the successful measurements and achievement of the results.

Appendix A. Supplementary data

Supplementary data to this article can be found online at https://doi.org/10.1016/j.ijhydene.2025.150321.

References

[1] Lohmann-Richters FP, Renz S, Lehnert W, Müller M, Carmo M. Review—challenges and opportunities for increased current density in alkaline electrolysis by increasing the operating temperature. J Electrochem Soc 2021;168(11):114501. https://doi.org/10.1149/1945-7111/ac34cc.
[2] Navarro RM, Guil R, Fierro JLG. Introduction to hydrogen production. In: Subramani V, Basile A, Veziroğlu TN, editors. *Woodhead Publishing series in energy*, number 83, *Compendium of hydrogen energy*. Cambridge, UK: Woodhead Publishing, an imprint of Elsevier; 2015. p. 21–61.
[3] Allebrod F, Chatzichristodoulou C, Mogensen MB. Alkaline electrolysis cell at high temperature and pressure of 250 °C and 42 bar. J Power Sources 2013;229:22–31. https://doi.org/10.1016/j.jpowsour.2012.11.105.
[4] Chatzichristodoulou C, Allebrod F, Mogensen MB. High temperature alkaline electrolysis cells with metal foam based gas diffusion electrodes. J Electrochem Soc 2016;163(11):F3036–40. https://doi.org/10.1149/2.0051611jes.
[5] Hodges A, et al. A high-performance capillary-fed electrolysis cell promises more cost-competitive renewable hydrogen. Nat Commun 2022;13(1):1304. https://doi.org/10.1038/s41467-022-28953-x.
[6] Swiegers GF, Terrett RNL, Tsekouras G, Tsuzuki T, Pace RJ, Stranger R. The prospects of developing a highly energy-efficient water electrolyser by eliminating or mitigating bubble effects. Sustain Energy Fuels 2021;5(5):1280–310. https://doi.org/10.1039/D0SE01886D.
[7] de Groot MT, Vreman AW. Ohmic resistance in zero gap alkaline electrolysis with a Zirfon diaphragm. Electrochim Acta 2021;369:137684. https://doi.org/10.1016/j.electacta.2020.137684.
[8] Haverkort JW, Rajaei H. Voltage losses in zero-gap alkaline water electrolysis. J Power Sources 2021;497:229864. https://doi.org/10.1016/j.jpowsour.2021.229864.
[9] Phillips R, Edwards A, Rome B, Jones DR, Dunnill CW. Minimising the ohmic resistance of an alkaline electrolysis cell through effective cell design. Int J Hydrogen Energy 2017;42(38):23986–94. https://doi.org/10.1016/j.ijhydene.2017.07.184.
[10] Kleinke MU, de Moraes MAB, Teschke O. A new type of PTFE-covered gas evolving electrode. J Electrochem Soc 1986;133(9):1815–8. https://doi.org/10.1149/1.2109028.
[11] Teschke O, Galembeck F. Effect of PTFE coverage on the performance of gas evolving electrodes. J Electrochem Soc 1984;131(5):1095–7. https://doi.org/10.1149/1.2115756.
[12] Heidrich H-J, Müller L. The effect of hydrophobic centres on the electrode surface on overvoltage in electrochemical gas evolution. Electrochim Acta 1990;35(6):1089–93. https://doi.org/10.1016/0013-4686(90)90047-4.
[13] Borodzinski J, Lasia A. Study of hydrogen evolution on selected PTFE-bonded porous electrodes. Int J Hydrogen Energy 1993;18(12):985–94. https://doi.org/10.1016/0360-3199(93)90080-T.
[14] Brussieux C, Viers P, Roustan H, Rakib M. Controlled electrochemical gas bubble release from electrodes entirely and partially covered with hydrophobic materials. Electrochim Acta 2011;56(20):7194–201. https://doi.org/10.1016/j.electacta.2011.04.104.
[15] Liu Y, Li S, Wu H, Shi Y. Experimental investigation and analysis for the bubble size distribution during alkaline water electrolysis by using a wire electrode. DeCarbon 2024;5:100052. https://doi.org/10.1016/j.decarb.2024.100052.
[16] Jiang X, et al. A novel multi-channel porous structure facilitating mass transport towards highly efficient alkaline water electrolysis. J Energy Chem 2024;93:511–8. https://doi.org/10.1016/j.jechem.2024.02.036.
[17] Winther-Jensen O, Chatjaroenporn K, Winther-Jensen B, MacFarlane DR. Towards hydrogen production using a breathable electrode structure to directly separate gases in the water splitting reaction. Int J Hydrogen Energy 2012;37(10):8185–9. https://doi.org/10.1016/j.ijhydene.2012.02.094.
[18] Marini S, et al. Advanced alkaline water electrolysis. Electrochim Acta 2012;82:384–91. https://doi.org/10.1016/j.electacta.2012.05.011.
[19] Xu W, Lu Z, Sun X, Jiang L, Duan X. Superwetting electrodes for gas-involving electrocatalysis. Acc Chem Res 2018;51(7):1590–8. https://doi.org/10.1021/acs.accounts.8b00070.
[20] Hosseini SR, Ghasemi S, Ghasemi SA. Effect of surfactants on electrocatalytic performance of copper nanoparticles for hydrogen evolution reaction. J Mol Liq 2016;222:1068–75. https://doi.org/10.1016/j.molliq.2016.08.013.
[21] Gomez M, et al. Unveiling OER bubble dynamics in alkaline electrolysis: impacts on cell resistance. Int J Hydrogen Energy 2025;106:138–45. https://doi.org/10.1016/j.ijhydene.2025.01.263.
[22] Bakker MM, Vermaas DA. Gas bubble removal in alkaline water electrolysis with utilization of pressure swings. Electrochim Acta 2019;319:148–57. https://doi.org/10.1016/j.electacta.2019.06.049.
[23] Iida T, Matsushima H, Fukunaka Y. Water electrolysis under a magnetic field. J Electrochem Soc 2007;154(8):E112. https://doi.org/10.1149/1.2742807.
[24] Matsushima H, Nishida T, Konishi Y, Fukunaka Y, Ito Y, Kuribayashi K. Water electrolysis under microgravity. Electrochim Acta 2003;48(28):4119–25. https://doi.org/10.1016/S0013-4686(03)00579-6.
[25] Crum LA. Acoustic cavitation series: part five rectified diffusion. Ultrasonics 1984;22(5):215–23. https://doi.org/10.1016/0041-624X(84)90016-7.
[26] Gillespie MI, van der Merwe F, Kriek RJ. Performance evaluation of a membraneless divergent electrode-flow-through (DEFT) alkaline electrolyser based on optimisation of electrolytic flow and electrode gap. J Power Sources 2015;293:228–35. https://doi.org/10.1016/j.jpowsour.2015.05.077.

[27] Tengattini A, et al. NeXT-grenoble, the neutron and X-ray tomograph in grenoble. Nucl Instrum Methods Phys Res Sect A Accel Spectrom Detect Assoc Equip 2020; 968:163939. https://doi.org/10.1016/j.nima.2020.163939.
[28] Schindelin J, et al. Fiji: an open-source platform for biological-image analysis. Nat Methods 2012;9(7):676–82. https://doi.org/10.1038/nmeth.2019.
[29] Arganda-Carreras I, et al. Trainable Weka Segmentation: a machine learning tool for microscopy pixel classification. Bioinformatics (Oxford, England) 2017;33(15): 2424–6. https://doi.org/10.1093/bioinformatics/btx180.
[30] Ershov D, et al. TrackMate 7: integrating state-of-the-art segmentation algorithms into tracking pipelines. Nat Methods 2022;19(7):829–32. https://doi.org/10.1038/s41592-022-01507-1.
[31] Vogt H. The actual current density of gas-evolving electrodes—notes on the bubble coverage. Electrochim Acta 2012;78:183–7. https://doi.org/10.1016/j.electacta.2012.05.124.
[32] Zhang D, Zeng K. Evaluating the behavior of electrolytic gas bubbles and their effect on the cell voltage in alkaline water electrolysis. Ind Eng Chem Res 2012;51 (42):13825–32. https://doi.org/10.1021/ie301029e.
[33] Rocha F, Delmelle R, Georgiadis C, Proost J. Effect of pore size and electrolyte flow rate on the bubble removal efficiency of 3D pure Ni foam electrodes during alkaline water electrolysis. J Environ Chem Eng 2022;10(3):107648. https://doi.org/10.1016/j.jece.2022.107648.
[34] Lickert T, et al. On the influence of the anodic porous transport layer on PEM electrolysis performance at high current densities. Int J Hydrogen Energy 2020;45 (11):6047–58. https://doi.org/10.1016/j.ijhydene.2019.12.204.
[35] LeRoy RL. Hydrogen production by the electrolysis of water: the kinetic and thermodynamic framework. J Electrochem Soc 1983;130(11):2158–63. https://doi.org/10.1149/1.2119544.
[36] Yuan S, et al. Bubble evolution and transport in PEM water electrolysis: mechanism, impact, and management. Prog Energy Combust Sci 2023;96:101075. https://doi.org/10.1016/j.pecs.2023.101075.
[37] Haug P, Koj M, Turek T. Influence of process conditions on gas purity in alkaline water electrolysis. Int J Hydrogen Energy 2017;42(15):9406–18. https://doi.org/10.1016/j.ijhydene.2016.12.111.
[38] Leonard E, et al. Operando X-ray tomography and sub-second radiography for characterizing transport in polymer electrolyte membrane electrolyzer. Electrochim Acta 2018;276:424–33. https://doi.org/10.1016/j.electacta.2018.04.144.
[39] Majasan JO, Cho JIS, Dedigama I, Tsaoulidis D, Shearing P, Brett DJL. Two-phase flow behaviour and performance of polymer electrolyte membrane electrolysers: electrochemical and optical characterisation. Int J Hydrogen Energy 2018;43(33): 15659–72. https://doi.org/10.1016/j.ijhydene.2018.07.003.
[40] Wang J. Theory and practice of flow field designs for fuel cell scaling-up: a critical review. Appl Energy 2015;157:640–63. https://doi.org/10.1016/j.apenergy.2015.01.032.
[41] Maier M, et al. Mass transport in polymer electrolyte membrane water electrolyser liquid-gas diffusion layers: a combined neutron imaging and X-ray computed tomography study. J Power Sources 2020;455:227968. https://doi.org/10.1016/j.jpowsour.2020.227968.